



ISAV

Journal of Theoretical and Applied
Vibration and Acoustics

journal homepage: <http://tava.isav.ir>



An investigation into the behaviour of resonances of polymeric and metallic cylinders in acoustic wave scattering

Vajihehsadat Sajadi ^a, Farhang Honarvar ^{a,*}, Mohammadreza Kari ^b

^a NDE Lab., Faculty of Mechanical Engineering, K.N. Toosi University of Technology, Tehran, IRAN.

^b Medical Physics, University of Wisconsin-Madison, Madison, Wisconsin 53705, USA

ARTICLE INFO

Article history:

Received 4 September 2025

Received in revised form
21 November 2025

Accepted 5 December 2025

Available online 2 June 2026

Keywords:

Acoustic wave scattering

Ultrasonic testing

Resonance frequencies

Polymer filament

Additive manufacturing

ABSTRACT

Accurate characterization of thin cylinders, such as polymer filaments and metal wires, is important for improving the performance of rapidly developing additive manufacturing (AM) processes. This study investigates the circumferential resonance frequencies of metallic and polymeric cylinders subjected to normally incident plane acoustic waves, enabling the identification of their key elastic properties. Using a combination of analytical techniques and experimental methods, the acoustic wave scattering of both material types is thoroughly examined. The analysis uncovers a clear distinction: in aluminum cylinders, resonance frequencies appear as minima in the form function, whereas in polymer filaments they appear as maxima. This contrasting behavior is validated through theoretical models and experimental measurements. Furthermore, the study examines interference at normal incidence and shows that the constructive interference responsible for resonances in the polymer filament appears as maxima (peaks) in the form function. In contrast, the destructive interference in the metallic cylinder manifests as minima (dips). This clear analytical and experimental demonstration of contrasting resonance behavior provides deeper insight into the acoustic properties of metallic and polymeric materials, thereby supporting improved material selection and quality control in AM applications.

Research Article

© 2025 Iranian Society of Acoustics and Vibration, All rights reserved.

* Corresponding author.

E-mail address: honarvar@kntu.ac.ir (F. Honarvar)

1. Introduction

This research is motivated by a compelling drive to address significant knowledge gaps and advance understanding of the acoustic behaviors of polymer filaments, which are commonly used in additive manufacturing processes. The goal of this study is to uncover the intricacies of the acoustic characteristics of such polymer filaments by comparing them to those of metal filaments. The increasing prominence of additive manufacturing underscores the urgent need for comprehensive insights into the acoustic properties of diverse materials used in these processes, as these properties can be used for material characterization and quality control. This study is propelled by an intrinsic desire to understand the manifestation of these acoustic behaviors and how this understanding can be translated into practical applications. By investigating and comparing the resonance frequencies of aluminum and Polylactic Acid (PLA) cylinders, the aim is not only to contribute to the theoretical foundations of material acoustic behavior but also to pave the way for real-world applications, particularly in non-destructive testing methods such as ultrasonic testing. Motivated by this, the research aims to catalyze advancements in material design, manufacturing processes, and applications, providing tangible benefits to industries that rely on additive manufacturing technologies.

In the fused filament fabrication (FFF) process, one of the most versatile additive manufacturing methods, the raw material is typically a small-diameter polymer filament that is not easily subjected to destructive tests, such as tensile testing. Hence, the creation of a Non-Destructive Evaluation (NDE) technique to assess the elastic characteristics of these filaments would be greatly advantageous. A promising NDE strategy could entail employing inverse methods, a methodology previously utilized in the analysis of metallic rods [1]. The underlying physics of acoustic wave interactions with an elastic entity is a multifaceted process that involves the emergence of diverse surface wave types within and around the elastic material. For instance, in the scenario of an elastic cylindrical entity, when acoustic waves encounter the boundary of the cylinder, they not only undergo reflection from the surface but also give rise to surface waves propagating along the perimeter of the cylinder. There is a close relationship between the resonance modes of an elastic object and the surface waves that travel along its boundary; this relationship can be used to characterize the object. If the frequency of the incoming wave matches one of the circumferential resonance frequencies of the cylinder, the phase matching of the surface waves leads to constructive interference. This phenomenon is evident in Resonance Scattering Theory (RST), first introduced by Überall et al. [1], which provides an initial physical explanation. According to resonance-scattering theory, the reflected signal from an elastic cylinder in a fluid has two components. The first component is a smooth background, and the second one is the cylinder's resonance frequencies. The normalized far-field pressure spectrum of an elastic cylinder, known as the *form function*, includes these two components. Resonances are denoted by two integers, n and l . Integer n indicates the mode number of the resonance, and l determines the type of surface wave generated around the cylinder. The form function can be measured using two experimental methods: the semi-harmonic method and the short-pulse MIIR [2], where MIIR stands for the Method of Isolation and Identification of Resonances.

The development of mathematical frameworks for understanding the scattering of acoustic waves from submerged cylinders has seen significant contributions from various researchers, some of which are reviewed here. Faran [3] introduced the initial mathematical framework, laying the groundwork for subsequent advancements in the field. Flax et al. [4] furthered this work by

developing a mathematical model specifically for the backscattering of acoustic waves from elastic submerged cylinders. Honarvar and Sinclair [5] introduced a model for the scattering of acoustic waves by anisotropic cylinders with hexagonal symmetry, characterized by five independent elastic constants. Ahmad and Rahman [6] investigated the scattering of acoustic waves by transversely isotropic cylinders, advancing understanding of complex wave interactions.

Flax et al. [1] analyzed resonance scattering of acoustic waves from both elastic cylinders and spheres, deconstructing the scattering function into constituent partial waves. Rhee and Park [7] proposed an innovative resonance formalism for the scattering of acoustic waves and compared it with classical resonance scattering theory. Hefner and Marston [8] analyzed backscattering enhancements from PMMA spheres in water, revealing pronounced resonance peaks in the form function f within the $ka = 1.5 - 7$ range. Their study elucidated these peaks as resulting from subsonic Rayleigh wave interactions coupled with acoustic tunneling, underscoring the spheres' significant target strength potential at lower frequencies. Schuetz and Neubauer [9] laid the groundwork for understanding acoustic reflections from both nonabsorbing and absorbing cylindrical structures, establishing a theoretical foundation for the role of absorption in acoustic scattering by cylinders. Building on this foundation, Mitri et al. [10] introduced a comprehensive expression for the backscattering form function of cylindrical targets exposed to an incident sound field, incorporating the absorption characteristics of shear and compressional waves in viscoelastic materials. Their numerical results highlighted the influence of ultrasonic absorption on the material properties of the cylinder. Williams and Marston [11] developed key concepts of phase sensitivity and resonance identification for spherical geometries, using the Sommerfeld-Watson transformation (SWT) to analyze backscattering and the Fabry-Perot analysis to explore resonance amplification. Their work demonstrated that the interference of the specular and Rayleigh contributions for a tungsten carbide sphere, within the range $10 \leq ka \leq 80$, produces the underlying structure in $|f(ka)|$. In contrast, whispering-gallery wave resonances produce a finer superposed structure [11]. Sun and Marston [12] extended this framework to cylindrical shells, emphasizing the role of leaky Lamb waves in the form-function structure. They demonstrated that mode conversion and leaky wave radiation dominate backscattering for $ka \geq 7$. Their analysis emphasized how the relative phase between the background (specular) contributions and guided waves determines whether resonances manifest as peaks or dips in the backscattering spectrum. Mitri et al. [13] further refined this resonance-based approach, demonstrating the sensitivity of absolute phase shifts in detecting resonances in both cylinders and spheres, thereby establishing its efficacy as a powerful tool for resonance analysis. While the geometries of spheres and infinite cylinders are distinct, the underlying scattering phenomena share critical similarities, a point emphasized in Marston's high-frequency scattering analyses [14, 15]. Batard and Quentin [16] contributed to the field by measuring elastic properties in submerged isotropic cylinders using a reverse technique applied to acoustic scattering data. They focused on the resonance frequency and bandwidth, derived from altering the elastic constants, to characterize the cylinders. Honarvar and Sinclair [17] explored the applications of resonance acoustic spectroscopy (RAS) in non-destructive evaluation and monitoring of cylindrical components. They developed mathematical models for elastic and viscoelastic rods with coatings, as well as transversely isotropic infinite cylinders, aligning theoretical predictions with experimental measurements to showcase the utility of RAS. Kari et al. [18] introduced an innovative non-destructive method for determining the elastic constants of transversely isotropic materials, solving an inverse problem based on scattering data. Furthermore, in another paper, Kari and Honarvar [19] measured the speed and density of

steel and aluminum rods, as well as a steel rod embedded in an aluminum matrix. They employed a genetic algorithm as an inverse method, validating their results with theoretical and empirical form functions.

These diverse contributions have enriched the understanding of acoustic wave scattering from cylinders, spanning from fundamental mathematical frameworks to practical applications in non-destructive evaluation and material characterization.

In this paper, the analysis of resonance frequencies and their role in the acoustic behavior of cylindrical objects made from metals or polymers is emphasized. The investigation begins with the resonance characteristics of aluminum cylinders, where these frequencies appear as dips (minima) in the form function due to destructive interference. The analysis then shifts to polymeric cylinders, such as PLA, where resonance frequencies align with peaks (maxima) in the form function, resulting from constructive interference. These contrasting behaviors highlight the fundamental differences in how resonance phenomena manifest in lightweight polymers compared to metals. Both analytical and experimental methodologies are presented to determine resonance frequencies and interference types, offering a systematic approach for evaluating these materials. The findings contribute valuable insights for the ultrasonic testing of polymer filaments in additive manufacturing, enabling real-time quality control and material characterization.

2. Theoretical model

In this section, the mathematical model of the scattering of a monochromatic plane harmonic acoustic wave from an elastic cylinder is briefly examined. Figure 1 illustrates an infinite monochromatic plane acoustic wave impinging on an infinitely long submerged cylinder at an incident angle α , with a frequency of $\omega/2\pi$. The variable α is retained throughout the formulation to preserve generality, although all subsequent results assume $\alpha = 0$. The cylinder's radius is a , its density is ρ , and the density of the surrounding fluid is ρ_w . The problem is solved in a cylindrical coordinate system (r, θ, z) , where the z -axis aligns with the axis of the cylinder. The pressure p_i of the longitudinal plane wave impinging on the cylinder at an arbitrary point M with coordinates (r, θ, z) is given by Equation 1 [4]:

$$p_i = p_0 \sum_{n=0}^{\infty} \varepsilon_n i^n J_n(k_{\perp} r) \cos(n\theta) e^{i(k_z z - \omega t)} \quad (1)$$

where p_0 is the amplitude of the impinging wave, ε_n is the Neumann factor (for $n = 0$, $\varepsilon_0 = 1$, and for $n \geq 1$, $\varepsilon_n = 2$), J_n is the first kind Bessel function of order n , k is the wave vector, $k_z = k \sin \alpha$, $k_{\perp} = k \cos \alpha$, and r is the position vector of point M . Furthermore, $|k| = \omega/c_w$ is defined such that ω is the angular frequency and c_w is the longitudinal wave speed in the fluid surrounding the cylinder. The scattered wave p_s of the cylinder at point M follows the wave equation and is calculated from the following equation [4]:

$$p_s = p_0 \sum_{n=0}^{\infty} \varepsilon_n i^n A_n H_n^{(1)}(k_{\perp} r) \cos(n\theta) e^{i(k_z z - \omega t)} \quad (2)$$

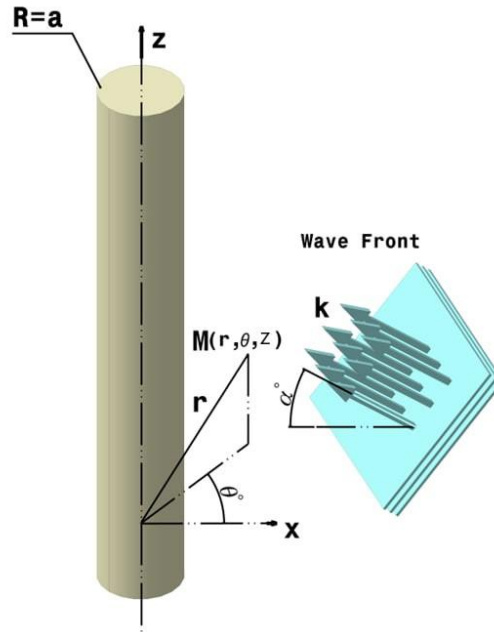


Fig. 1. Geometric principles in theoretical analysis (plane wave incidence)

The coefficients A_n are taken from Ref. [5]. The scattered pressure field is usually calculated at a far field ($r \gg a$) for a fixed angle θ for a range of frequencies. The resulting far-field amplitude spectrum is called the *form function* and is obtained from the following equation [20]:

$$f_{\infty}(\theta, ka) = \left(\frac{2r}{a}\right)^{\frac{1}{2}} \left(\frac{p_s}{p_0}\right) e^{-ik_{\perp}r} \quad (3)$$

The form function is written as the sum of individual normal modes:

$$f_{\infty}(\theta, ka) = \sum_{n=0}^{\infty} f_n(\theta, ka) \quad (4)$$

hence, the normal modes for each n are defined as follows [20]:

$$f_n(\theta, ka) = \frac{2}{\sqrt{i\pi ka}} \epsilon_n A_n \cos(n\theta) \quad (5)$$

Using the resonance scattering theory (RST), which shows that the reflected amplitude spectrum from an elastic scatterer is a combination of resonant components placed on a smooth background [1], several researchers [1, 7] have obtained the resonance information of the scatterers by simply subtracting the appropriate background term (rigid, soft, or intermediate) from the overall scattered pressure field. According to Ref. [21], the background term may correspond to a rigid body, a soft body (e.g., air bubbles), or an intermediate background (e.g., thin-walled elastic shells) [21]. If the density of the target material is much greater than the density of the surrounding fluid, in this case water, Equations (6) and (7) for a rigid cylinder should be used. The background term may correspond to the component for a rigid body, an acoustically soft body (e.g., air bubbles), or an intermediate background (e.g., thin-walled elastic shells) [21]. Therefore, a rigid reference cylinder

is utilized in this study. It should be noted that in the case of intermediate backgrounds, the phase of the background contribution can vary with ka , as discussed in [12, 22]. While the current analysis uses the rigid background model as described in Ref. [21], this distinction is acknowledged here for completeness.

$$f_n^{res}(\theta) = \frac{2}{\sqrt{i\pi ka}} \varepsilon_n (A_n - A_n^r) \cos(n\theta) = f_n - f_n^r \quad (6)$$

Where A_n^r and f_n^r are the scattering coefficients of the rigid background and its form function, respectively, which are determined as per Equation 7 [20].

$$f_\infty^r = -\frac{2}{\sqrt{i\pi ka}} \sum_{n=0}^{\infty} \varepsilon_n \frac{J'_n(ka)}{H_n^{(1)'}(ka)} \cos n\theta \quad (7)$$

(for cylinder with a rigid background)

Where, J'_n and $H_n^{(1)'}$ are the derivatives of the Bessel and Hankel functions of the first kind of order n with respect to ka , respectively.

This equation, known as classical RST, appears to provide accurate estimates of the resonance frequencies [7]. The background constituent of the form function interacts with Rayleigh and whispering-gallery waves to produce a series of interference patterns [23]. For metallic targets, the circumferential elastic amplitudes are largely 180 degrees out of phase with the background, resulting in interference minima. In contrast, interference in lightweight targets like Lucite is largely constructive, leading to the formation of interference peaks [23]. To determine the interference type, the phase difference between the resonance spectrum and the rigid background is measured, and its cosine is calculated. The concept of using the cosine of the phase difference to determine constructive or destructive interference comes from fundamental wave interference principles in physics [24]. Constructive interference occurs when the phase difference between two waves (ϕ) is an integer multiple of 2π , meaning the waves are in phase and their amplitudes add up, resulting in a larger resultant amplitude [24]. Mathematically, when $\cos(\phi) \geq 0$, it indicates constructive interference. Destructive interference occurs when the phase difference is an odd multiple of π , where the waves are out of phase, and their amplitudes tend to cancel out each other, resulting in a smaller resultant amplitude. Mathematically, destructive interference is indicated when $\cos(\phi) < 0$ [24]. Thus, if this cosine value is greater (or equal) to zero, the interference is constructive; otherwise, it is destructive.

In addition to the above method, Flax et al. [1] also classified resonances as Type *A*, *B*, and *C* based on resonance terms and their interference conditions in the partial wave amplitude equation [1]:

$$f_n(\theta, ka) = \frac{2i}{\sqrt{i\pi ka}} e^{2i\xi_n^r} \varepsilon_n \left[\frac{\frac{1}{2}\Gamma_n^r}{ka_n^r - ka - \frac{1}{2}i\Gamma_n^r} - e^{-i\xi_n^r} \sin \xi_n^r \right] \cos(n\theta) \quad (8)$$

where Γ_n^r introduced as resonance width [1]:

$$(9)$$

$$\tan \xi_n^r = \frac{J'_n(ka)}{H_n^{(1)'}(ka)}$$

(for rigid reference cylinder)

Type A resonances are classified as "pure" resonances or constructive interference. These resonances occur at frequencies nearly coinciding with a null of the rigid background, where $\xi_n^r \cong 0$ where, ξ_n^r is the *phase shift* and can be determined as per Equation 9 [1]. Therefore, in these cases, only the resonance contribution in f_n , as shown in Equation 8, is significant. Type B resonances, on the other hand, are classified as destructive resonances, with $\xi_n^r \cong \frac{\pi}{2}$. This results in the background term in Equation 8 becoming $-i$, while the resonance term at $ka = ka_n^r$ becomes $+i$, leading to a cancellation effect [1]. Type C resonances do not coincide with peaks nor dips of the background [1].

Polymer filaments, as polymeric materials, exhibit viscoelastic behavior [25] characterized by complex elastic coefficients. Here, the real part denotes the material's elastic properties, while the imaginary part reflects its damping characteristics. This study aims to identify resonance frequency locations in the form function for material characterization. Despite damping effects from ultrasonic absorption reducing the amplitude in polymer filaments, the resonance frequencies do not shift within the filament's frequency spectrum. It is important to note that for the calculation of a form function, this paper does not account for acoustic attenuation, which may be relatively high in PLA. Therefore, while the focus remains on determining resonance frequency locations, excluding acoustic attenuation factors from these calculations does not affect the objectives of this study [10].

3. Experimental method

The short-pulse MIIR is used to measure the form function, resonance spectrum, and resonance frequencies of the cylindrical samples studied in this paper [26]. In short-pulse MIIR, the target is excited by a short pulse, the duration of which is small compared to the diameter of the target divided by the speed of sound [26]. In Resonance Acoustic Spectroscopy (RAS), the target is positioned sufficiently far from the probe to satisfy the far-field conditions. These simplifications are well-established practices in acoustics, ensuring a practical and accurate representation of real-world scenarios in which far-field conditions are commonly encountered [27].

The first echo, the specular echo, can be used to calibrate the system [26]. The form function is obtained by taking the Fast Fourier Transform (FFT) of the backscattered signal [26]. To compare the analytical and experimental form functions, the effects of the transmitter and receiver transfer functions must be removed by utilizing a deconvolution process. This process is performed according to the procedure presented by Sodagar et al.[26]. To separate the effects of the measurement system and obtain an experimental form function, a reference frequency spectrum that excludes resonance effects is required². Sodagar et al.[26] isolated the specular echo reflected from the cylinder from the total backscattered signal and then used its frequency spectrum as the reference spectrum. To eliminate the effects of the measurement system, the following equation is used [26]:

$$|f_{\infty}| = \left(\frac{1}{\cos\alpha}\right)^{1/2} \left|\frac{S(\omega)}{S'(\omega)}\right| |f_{\infty}^r| \tag{10}$$

where, $S(\omega)$ is the frequency spectrum of the cylinder and $S'(\omega)$ is the frequency spectrum of the specular echo, and $|f_{\infty}^r|$ is the analytical form function obtained from a reference cylinder by using equation 7.

In this paper, the experimental frequency spectra for both a metal and a polymer, as detailed in Table 1, are plotted. The locations of the resonance frequencies are examined and determined based on whether the reference cylinder is rigid or soft.

The data acquisition system used in this study consists of an analog-to-digital card that is installed on the main board of a computer. This card, model CS14100-1M, manufactured by Gage, is a 14-bit card with a sampling frequency (f_s) of 100 megasamples per second. It has one channel at 100 Ms/s and two channels at 50 Ms/s, with a signal-to-noise ratio of 63 dB. Bandwidth is measured by examining the frequency spectrum of the specular echo using the Full Width at Half Maximum (FWHM) [28]. The ultrasonic transducer used in the experiments is a flat circular immersion transducer with a central frequency of 1 MHz and a diameter of 12.7 mm. The 1-megahertz transducer has a bandwidth ranging from 500 to 1500 kHz. The test specimens, consisting of aluminum and PLA, were immersed in water maintained at 25°C, as shown in Figure 2. The aluminum sample and PLA filament have diameters of 4 mm and 1.76 mm, respectively. To minimize end effects, both samples were selected to be 30 cm long [29]. Although the ideal sample length for such tests is typically infinite or at least semi-infinite length [12], some studies [18] have explicitly used a 300-mm sample length and obtained reliable results. Due to experimental limitations, the strict far-field criterion specified in Equation 1 of Ref. [30] could not be met. However, the less restrictive criterion of $r \gg k(a^2)$ [31], has been met, allowing us to treat the wavefronts as planar in our study.

In the experimental setup shown in Figure 2, the cylinder was positioned at a right angle to the transducer's axis by aligning it with the transducer holder. This alignment allowed for consistent visual inspection of the signal shape to ensure accuracy. Furthermore, the filament piece was carefully held with precise drilling constraints, and the signal quality was consistently monitored. After immersing the target, sufficient time was allowed for all bubbles to dissipate before commencing the tests and recording signals naturally.

Table 1. Specifications of the materials used in tests based on the manufacturer's data

Material	Density (kg/m ³)	Sample Type	Diameter (mm)	Longitudinal Wave Velocity (m/s)	Transverse Wave Velocity (m/s)
Aluminum	2776	Cylinder	4	6265	2815
PLA	1250	Filament	1.76	2062 (Ref. [29])	1112 (Ref. [29])
Water	1000	---	---	1480	---

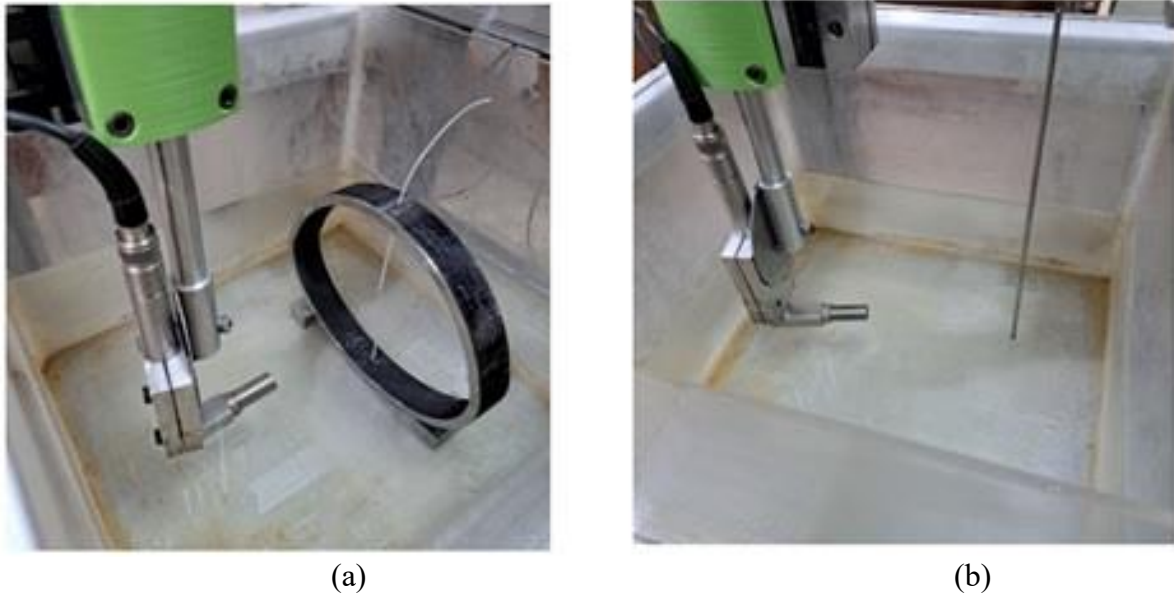


Fig. 2. a) Aluminum cylinder; b) polymer filament

4. Results and discussion

The primary objective of this paper is to locate the resonance frequencies and the type of interference of these resonance frequencies with the background part of the form function.

A. Theoretical results

In this section, a metallic aluminum cylinder is examined first. The properties of aluminum are listed in Table 1, and graphs of the theoretical form function of this aluminum cylinder are plotted for $\theta = \pi$ in Figure 3 based on Equation 4. In the calculation of the form function, the summation over partial waves is truncated at $n = 30$, following the approach of Rhee and Park [7]. This ensures numerical convergence while maintaining computational efficiency. In this study, amplitudes were normalized by their respective maximum values to showcase relative variations across frequencies. This method was chosen to facilitate clearer comparative analysis and highlight frequency-dependent variations in the data.

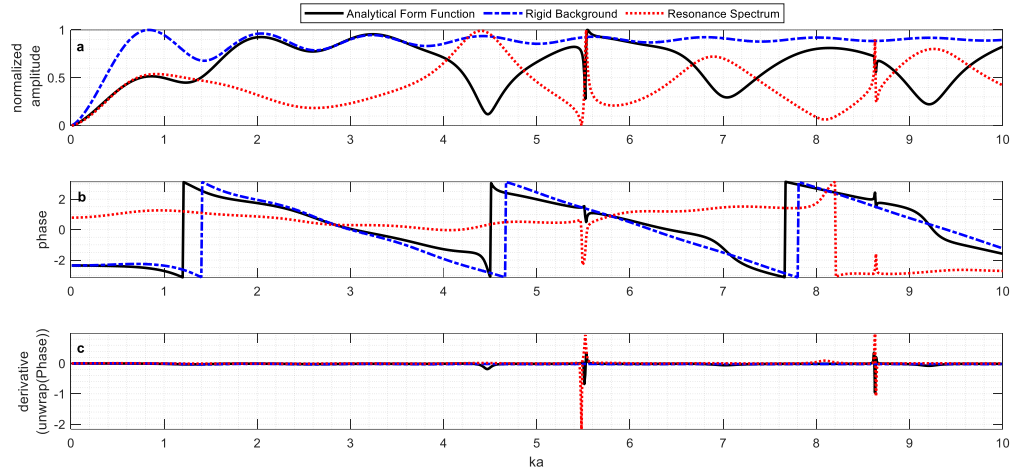


Fig. 3. Analytical graphs of the aluminum cylinder: a) amplitude plots of the form function, rigid background, and resonance spectrum; b) phase plots of the form function, rigid background, and resonance spectrum; c) derivative of the unwrapped phase plots of the form function, rigid background, and resonance spectrum.

Figure 3 includes three distinct groups of plots. Figure 3a shows the magnitudes of the form function, rigid background, and resonance spectrum. Figure 3b shows the phases of these functions, while Figure 3c presents the derivatives of the unwrapped phase of these functions by employing the methodology described in Ref. [29]. This visual representation is utilized to pinpoint resonance points through established resonance equations.

It is well known that the resonance frequencies of an aluminum cylinder are precisely positioned at the minima of the form function [19]. Upon scrutiny of the graphs shown in Figure 3a, it becomes evident that the resonance points, aligning precisely with the minima of the form function, correspond to the local peaks observed in the resonance spectrum. These points, graphically represented on the rigid background diagram, are meticulously classified as minimum, maximum, or non-peak. Table 2 shows how resonances appear as the minima of the form function.

Table 2. Description of the extreme points of the analytical form function of the aluminum cylinder

ka	Position on form function	Position on rigid response	Position on the resonance spectrum	Interference type	Resonance width (FWHM)	(<i>n, l</i>) (Ref. [19])	Interference (Ref. 1)
4.47	Min.	Max.	Max.	Destructive	1.18	(2,1)	Destructive – Type B
5.52	Min.	Non.Peak	Max.	Destructive	0.05	(1,2)	Pure Resonance – Type A
7.04	Min.	Non-Peak	Max.	Destructive	1.28	(3,1)	Destructive – Type B
8.64	Min.	Min.	Max.	Destructive	0.04	(2,2)	Destructive – Type B
9.21	Min.	Max.	Max.	Destructive	1.31	(4,1)	Pure Resonance – Type A

The initial column lists the ka values associated with the resonance frequencies [19], followed by columns 2, 3, and 4, which pinpoint the precise locations of each data point on the form function, rigid background, and resonance spectrum, respectively. The next column sheds light on the phase interference calculated based on $\cos(\phi)$ [24], explained in Section 2. Furthermore, the resonance width, extracted from the resonance spectrum through the determination of the FWHM of the resonance peaks, is also recorded in Table 2, column 6. Each resonance frequency is represented by a pair of integers [27], n and l , where n denotes the resonance mode number and l signifies the serial number of that mode, cataloged in column 7 of Table 2 [19]. Lastly, column 8 specifies the interference type based on the mode-specific rigid background (not the total rigid background) following Ref. [1] and the discussion in Section 2. The classification is determined using the approach described by Flax et al [1], after identifying mode numbers (n, l) , as shown in the table.

The examination of the data in Table 2 corroborates this assertion, particularly evident in the resonance points at 5.52 and 8.64, where l equals 2, which exhibit notably narrower widths than other resonance modes. Furthermore, the comprehensive analysis detailed in Table 2 reveals that the phase interference observed in the aluminum cylinder is inherently destructive, as highlighted in column 5. At the same time, two pure resonances are distinctly identified in the last column, as explained in Ref. [1].

After thoroughly exploring the characteristics and resonant behaviors of aluminum as a metallic material, the focus now shifts to the analysis of a polymer material. The rest of this discussion aims to shed light on the distinctive properties and resonance phenomena displayed by PLA material. According to Ref. [23], the resonance frequencies of lightweight materials such as PLA are mostly located at the maxima of the form function due to constructive interference. This hypothesis will be examined in the subsequent discussion.

The methodology used for aluminum is employed to determine the resonance frequencies of a PLA filament. Instead of the form function, the partial wave modes are utilized to identify the (n, l) values for this polymer material. Figures 5 to 12 depict the partial wave graphs for each individual mode ranging from $n = 2$ to $n = 9$. Each figure is divided into three subplots. Subplot *a* illustrates the amplitudes of the partial wave, the rigid background, and the resonance spectrum. Subplots *b* and *c* showcase the phase and the derivative of the unwrapped phase of these parameters, respectively. The potential resonance frequencies at each n value are labeled, and their occurrences in different graphs are analyzed in Table 3.

In this analysis, the following methodology is used to identify the resonance frequencies for each n value of the polymer filament:

1. Identification of maximum or minimum points:

- The maximum and minimum points in the partial wave amplitude are located.
- The positions of these points are determined within the resonance spectrum and on a rigid background.

2. Determination of interference type and (n, l) values:

- The (n, l) values are identified, and the methods described in Refs. [24] and [1] are applied to determine the type of interference present.

- Any points with ambiguous interference characteristics between their partial wave resonance and the rigid background are excluded.

3. Checking for phase derivative peaks:

- The derivative of the unwrapped phase is crucial in acoustic resonance spectroscopy for highlighting resonance peaks [29].
- This derivative indicates where the phase changes most rapidly, as resonance peaks often cause sudden phase transitions, making them prominent in the derivative graph.
- By examining these peaks in the derivative graph, resonance frequencies can be identified effectively.

4. Identification of potential resonance frequencies:

- Sharp peaks in the phase derivative graph, corresponding to extreme points in both the partial-wave amplitude and the resonance spectrum, indicate potential resonance frequencies.
- The phase derivative graphs (Figures 5 to 12-subplot c) clearly show these resonance points as distinct peaks.
- Any other spikes in the derivative graphs that do not align with peaks or dips in the partial wave amplitude and resonance spectrum are considered abrupt changes and are disregarded.

5. Final determination of resonance frequencies:

- Points meeting the established criteria are classified as potential resonance frequencies for the specific n value and are recorded in Table 3.
- Importantly, points that do not correspond to extreme points of the overall form function (Figure 4) are excluded, even if they show maximum or minimum values in the partial wave amplitude spectrum.
- The final resonance frequencies are then determined based on the points that satisfy these criteria and are listed in Table 4.

This systematic approach ensures a focused analysis of the most relevant data, offering a precise insight into the material's resonance properties.

Figure 4 displays the form function, rigid background, and resonance spectrum of the PLA filament in subplot *a*, as well as the phase and phase derivative of the unwrapped phase of these functions in subplots *b* and *c*, respectively.

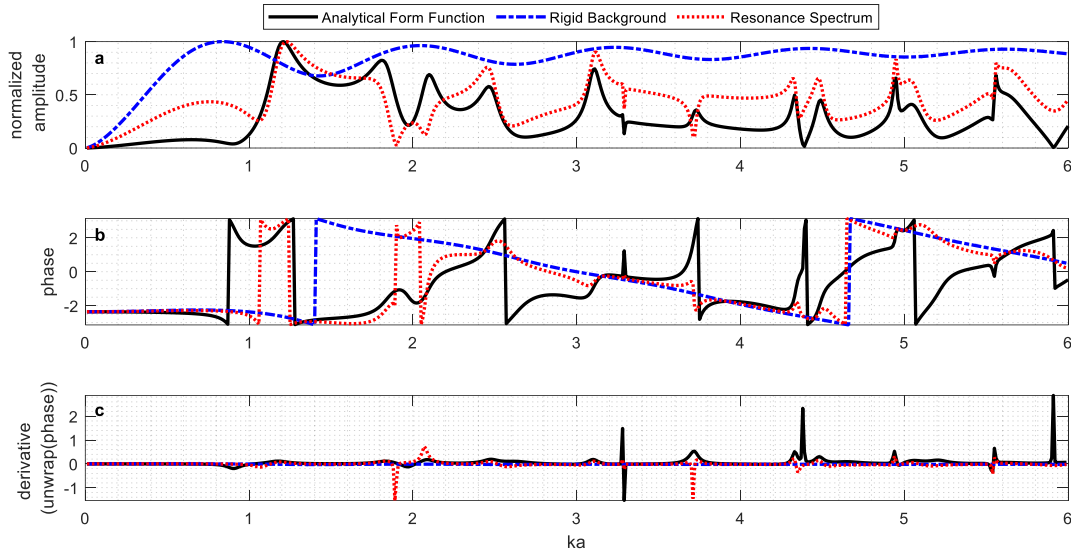


Fig. 4. Analytical graphs of the PLA filament; a) amplitude plots of the form function, rigid background, and resonance spectrum; b) phase plots of the form function, rigid background, and resonance spectrum; c) derivative of the unwrapped phase plots of the form function, rigid background, and resonance spectrum

In this analysis, the partial modes $n = 2$ to $n = 9$ are considered. Starting with $n = 2$, see Figure 5, the first resonance is observed at $ka = 1.19$, aligning with maximum points in both the partial wave amplitude and resonance spectrum. However, since this point does not correspond to an extremum of the overall form function (Figure 4), it is not a true resonance, and therefore it is disregarded in this analysis. Moving to $ka = 3.29$ in Figure 5, another maximum point emerges in both the partial wave amplitude and resonance spectrum, accompanied by a sharp peak in the phase derivative graph (Figure 5c), indicative of a potential resonance mode.

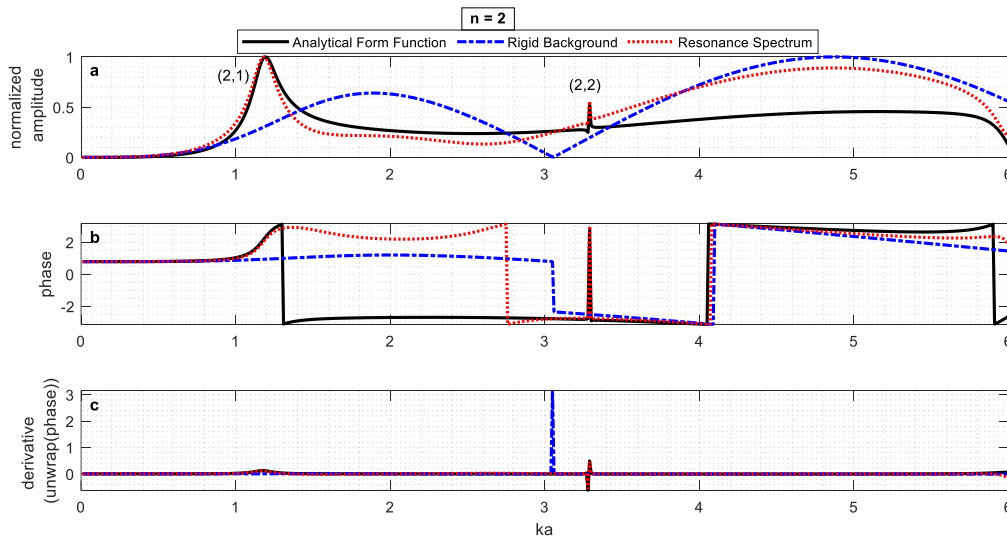


Fig. 5. Analytical graphs of partial mode of the PLA filament for $n = 2$; a) amplitude plots of the form function, rigid background, and resonance spectrum; b) phase plots of the form function, rigid background, and resonance spectrum; c) derivative of the unwrapped phase plots of the form function, rigid background, and resonance spectrum.

For $n = 3$ as shown in Figure 6, one resonance is observed at $ka = 4.43$, coinciding uniquely with a minimum in the overall form function. The point at $ka = 1.86$ is omitted due to the absence of a corresponding maximum or minimum in the form function.

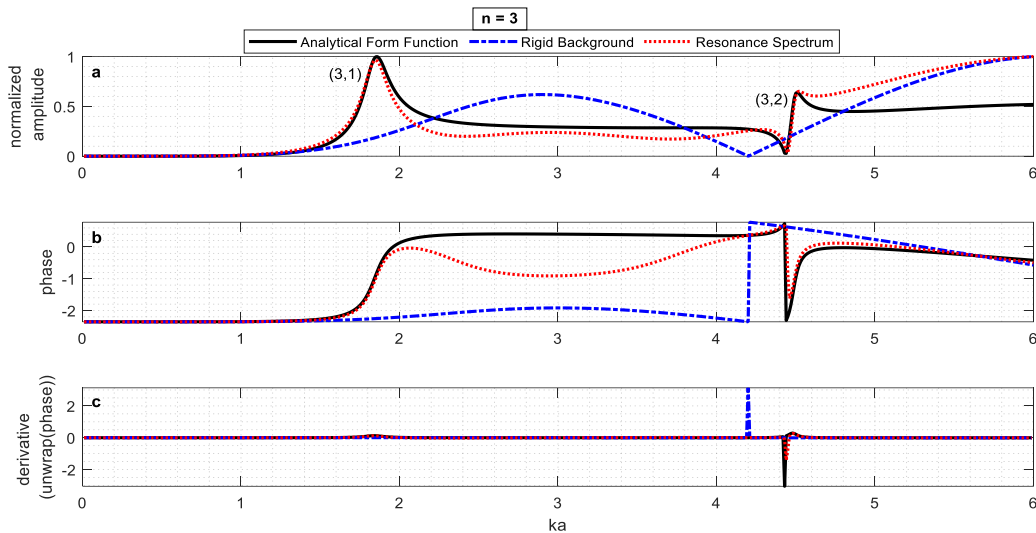


Fig. 6. Analytical graphs of partial mode of the PLA filament for $n = 3$; a) amplitude plots of the form function, rigid background, and resonance spectrum; b) phase plots of the form function, rigid background, and resonance spectrum; c) derivative of the unwrapped phase plots of the form function, rigid background, and resonance spectrum.

Moving on to $n = 4$ in Figure 7, two rapid changes are observed at $ka = 2.49$ and $ka = 5.44$. However, $ka = 5.44$ is disregarded as a resonance frequency due to the absence of a corresponding maximum or minimum in the form function.

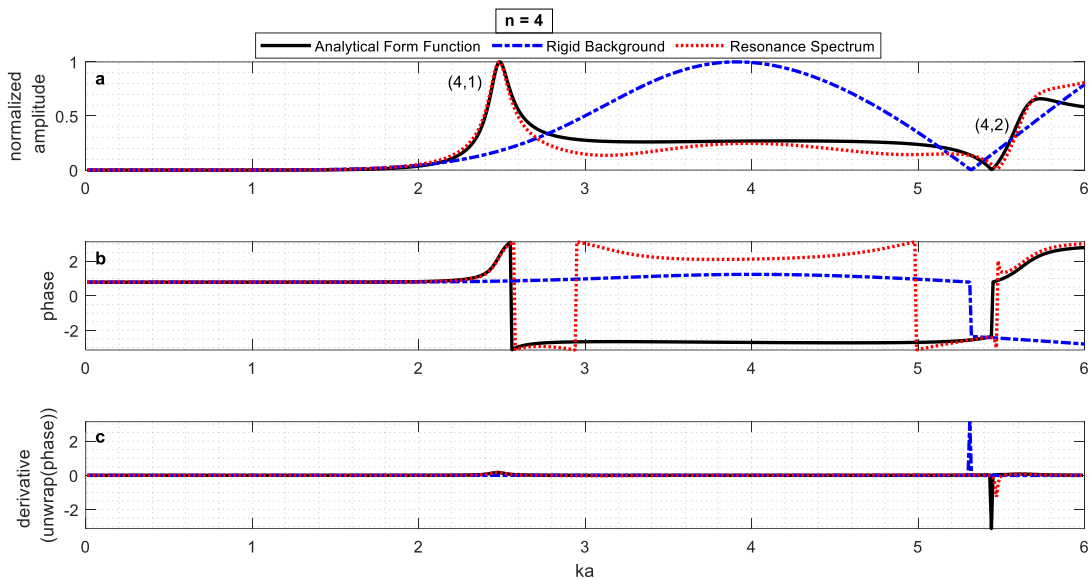


Fig. 7. Analytical graphs of partial mode of the PLA filament for $n = 4$; a) amplitude plots of the form function, rigid background, and resonance spectrum; b) phase plots of the form function, rigid background, and resonance spectrum; c) derivative of the unwrapped phase plots of the form function, rigid background, and resonance spectrum.

For $n = 5$, as shown in Figure 8, a pronounced resonance peak appears at $ka = 3.1$ in both the resonance and partial wave amplitudes, which is accompanied by a distinct peak in the phase derivative graph.

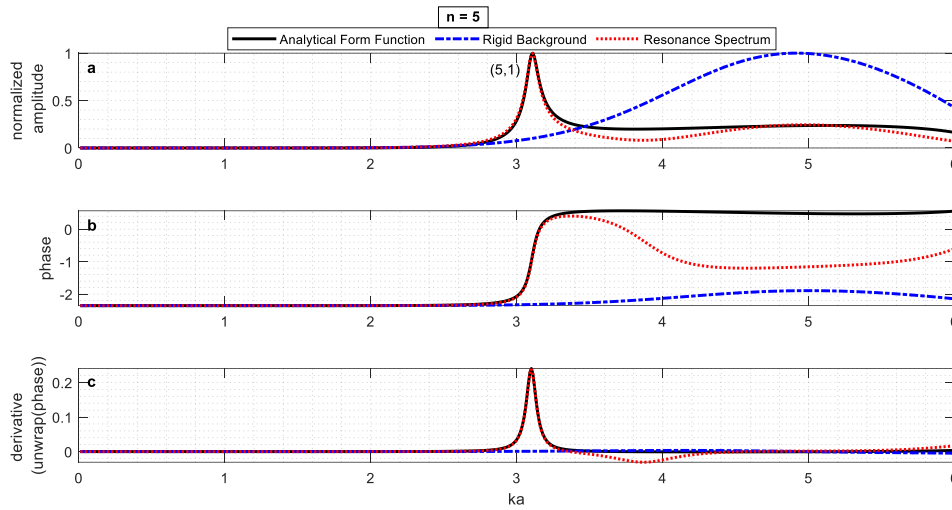


Fig. 8. Analytical graphs of partial mode of the PLA filament for $n = 5$; a) amplitude plots of the form function, rigid background, and resonance spectrum; b) phase plots of the form function, rigid background, and resonance spectrum; c) derivative of the unwrapped phase plots of the form function, rigid background, and resonance spectrum.

For $n = 6$, as indicated in Figure. 9, resonance is notably observed at $ka=3.72$, showcasing an alignment between the partial-wave amplitude and resonance characteristics, indicative of strong resonance behavior. Conversely, the dip observed at $ka = 4.6$, as shown in Figure 9c, is disregarded due to its ambiguous nature in the interference between the rigid background and resonance spectrum and its absence in Figure 4a.

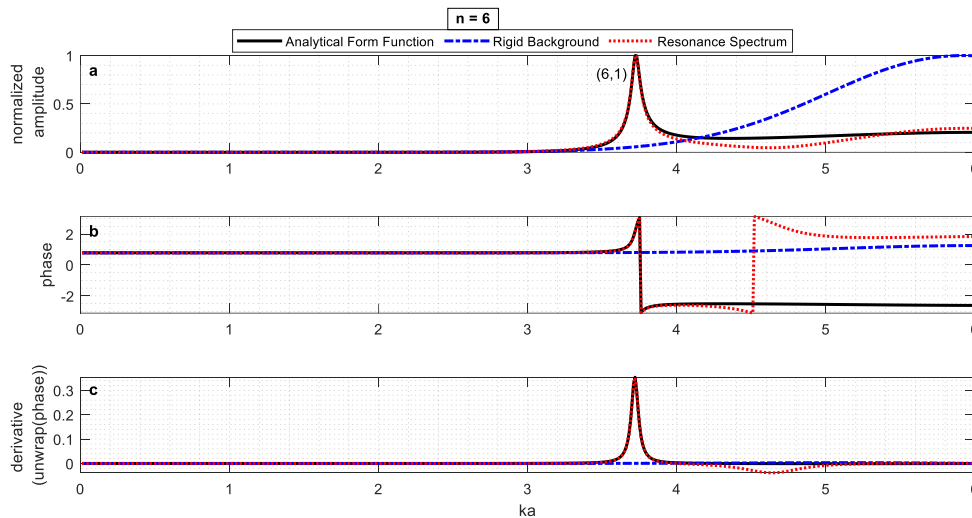


Fig. 9. Analytical graphs of partial mode of the PLA filament for $n = 6$; a) amplitude plots of the form function, rigid background, and resonance spectrum; b) phase plots of the form function, rigid background, and resonance spectrum; c) derivative of the unwrapped phase plots of the form function, rigid background, and resonance spectrum.

For $n = 7$, as shown in Figure 10, resonance manifests at $ka = 4.34$, marking another significant resonance behavior.

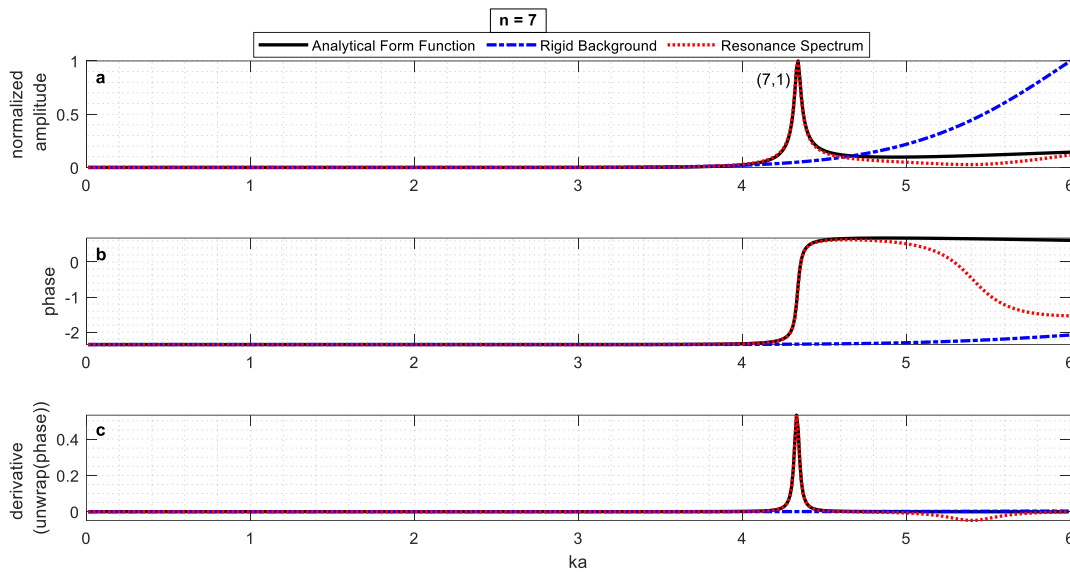


Fig. 10. Analytical graphs of partial mode of the PLA filament for $n = 7$; a) amplitude plots of the form function, rigid background, and resonance spectrum; b) phase plots of the form function, rigid background, and resonance spectrum; c) derivative of the unwrapped phase plots of the form function, rigid background, and resonance spectrum.

Similarly, for $n = 8$, as per Figure 11, resonance singularly manifests at $ka = 4.95$, highlighting its significance in the material's resonance response.

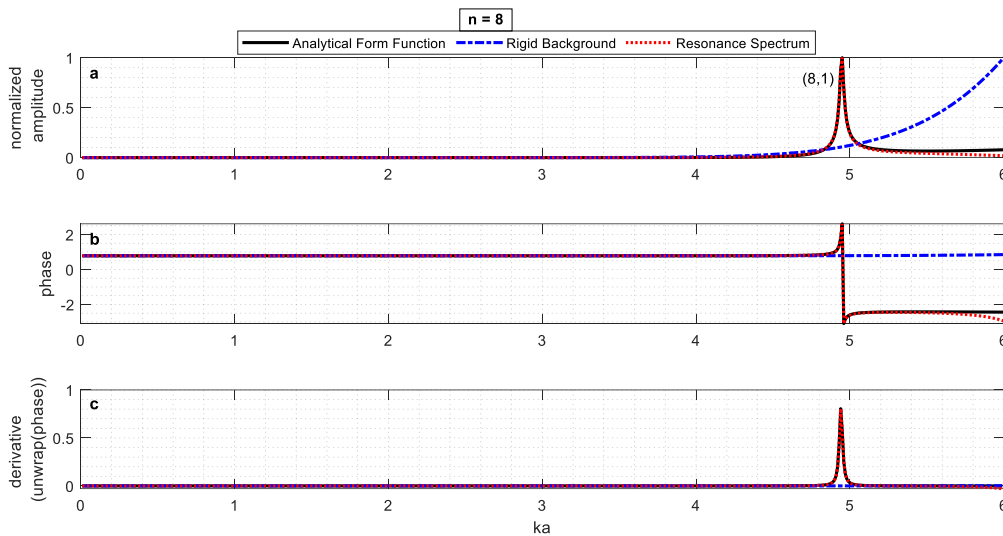


Fig. 11. Analytical graphs of partial mode of the PLA filament for $n = 8$; a) amplitude plots of the form function, rigid background, and resonance spectrum; b) phase plots of the form function, rigid background, and resonance spectrum; c) derivative of the unwrapped phase plots of the form function, rigid background, and resonance spectrum.

Lastly, for $n = 9$, as shown in Figure 12, resonance uniquely occurs at $ka = 5.55$, emphasizing another crucial resonance behavior.

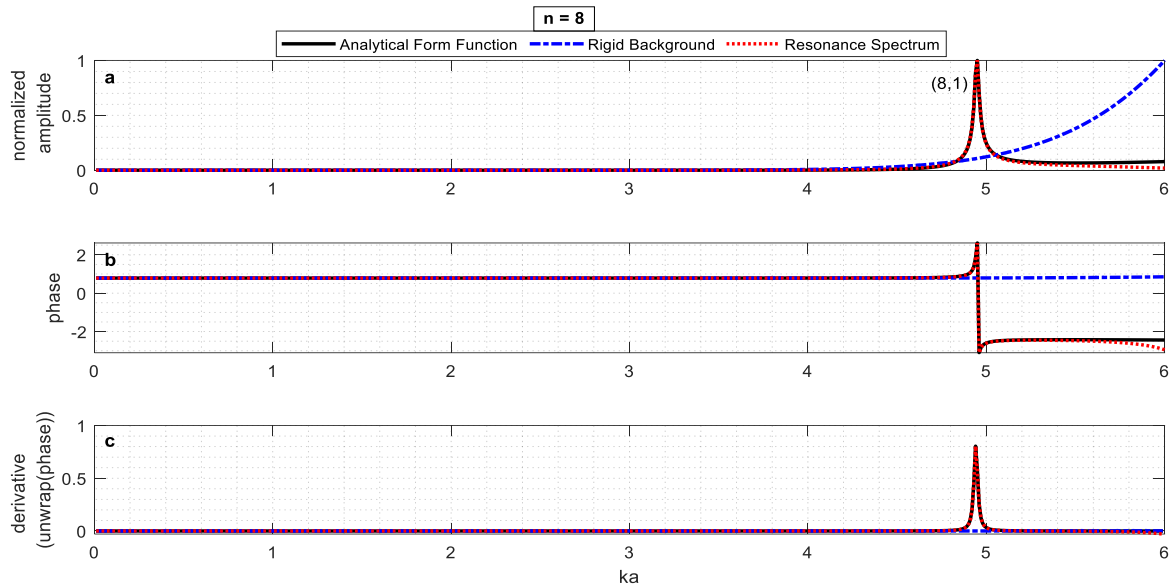


Fig. 12. Analytical graphs of partial mode of the PLA filament for $n = 9$; a) amplitude plots of the form function, rigid background, and resonance spectrum; b) phase plots of the form function, rigid background, and resonance spectrum; c) derivative of the unwrapped phase plots of the form function, rigid background, and resonance spectrum.

The comprehensive analysis of resonance characteristics for $n = 2$ to $n = 9$ is summarized in Table 3, detailing the key points of interest. The table indicates the precise location of points on the partial wave amplitude, rigid background, and resonance spectrum for each n value. The interference type, determined from the values of $\cos(\phi)$, is also outlined in column 5 of Table 3. Additionally, the corresponding values of (n, l) and resonance widths are specified in columns 6 and 7, respectively, providing further information regarding the observed resonance behavior.

Table 3. Characteristics of the extreme points of the partial modes of the analytical form function of the PLA filament

ka	Position on form function	Position on rigid response	Position on the resonance spectrum	Interference type	(n, l)	Resonance width
n = 2						
1.19	Maximum	Non.Peak	Maximum	Constructive	(2,1)	0.28
3.28	Minimum	Non.Peak	Minimum	Constructive	(2,2)	0.09
n = 3						
1.86	Maximum	Non.Peak	Maximum	Constructive	(3,1)	0.27
4.43	Minimum	Non.Peak	Minimum	Constructive	(3,2)	4.93
n = 4						
2.49	Maximum	Non.Peak	Maximum	Constructive	(4,1)	0.21
5.44	Minimum	Non.Peak	Minimum	Destructive	(4,2)	4.44
n = 5						
3.1	Maximum	Non.Peak	Maximum	Constructive	(5,1)	0.15
n = 6						
3.72	Maximum	Non.Peak	Maximum	Constructive	(6,1)	0.11
n = 7						
4.34	Maximum	Non.Peak	Maximum	Destructive	(7,1)	0.08
n = 8						
4.95	Maximum	Non.Peak	Maximum	Destructive	(8,1)	0.05
n = 9						
5.55	Maximum	Non.Peak	Maximum	Constructive	(9,1)	0.04

Following the analysis of partial modes, the maxima and minima of the form function can be extracted, and their positions in the rigid background graph and resonance spectrum, as well as their phase interference, can be examined. The results of this examination are compiled in Table 4, which is prepared in a manner entirely like that described for Table 2 earlier.

Table 4. Description of the extreme points of the analytical form function of the PLA cylinder

ka	Position on form function	Position on rigid response	Position on the resonance spectrum	Interference type	Resonance width (FWHM)	(n, l) [19]	Interference [1]
2.46	Max.	Non.Peak	Max.	Constructive	0.41	(4,1)	Pure Resonance – Type A
3.11	Max.	Non.Peak	Max.	Constructive	1.62	(5,1)	Pure Resonance – Type A
3.73	Max.	Non-Peak	Min.	Destructive	4.1	(6,1)	Pure Resonance – Type A
4.34	Max.	Non.Peak	Max.	Constructive	0.62	(7,1)	Pure Resonance – Type A
4.95	Max.	Non.Peak	Max.	Constructive	0.47	(8,1)	Pure Resonance – Type A
5.56	Max.	Non.Peak	Max.	Constructive	0.04	(9,1)	Pure Resonance – Type A
3.29	Min.	Non.Peak	Min.	Constructive	0.07	(2,2)	Pure Resonance – Type A
4.39	Min.	Maximum	Min.	Constructive	2.28	(3,2)	Pure Resonance – Type A

In Table 4, the points identified by analysis of the partial wave amplitude graphs and the form function largely align with maximum points of the form function, except for two points, i.e., $ka = 3.29$ and $ka = 4.39$. These two points pertain to whispering gallery modes (2,2) and (3,2). Despite demonstrating constructive interference, these modes appear as distinct minima. This intriguing phenomenon suggests a nuanced relationship between the geometric symmetry of the cylindrical targets and the resulting interference patterns. Whispering gallery modes are known for their symmetry and their tendency to exhibit constructive interference. The unexpected appearance of these modes as minima could imply subtle yet critical influences of mode orientation or asymmetries within the cylindrical geometry. Moreover, the fact that these points represent minima in both the form function and the resonance spectrum itself suggests a unique mechanism driving constructive interference under specific conditions. Further exploration is warranted to elucidate the mechanisms underlying this inversion of expected interference patterns. Investigating how geometric symmetries, such as mode shape and orientation, interact with incident acoustic waves could provide deeper insights into the complex wave dynamics within cylindrical structures.

Moreover, the phase interference at these points suggests that constructive interference has been observed in many cases, except for one instance at point ($ka = 3.73$). This point aligns with the maximum of the form function while coinciding with a minimum on the resonance spectrum. In addition, the final column relies on the resonance category as outlined in [1], which may be interpreted as pure resonance rather than as constructive interference.

In the Flax et al. model, Type A resonance corresponds to pure resonance, in which scattered waves combine in phase to produce a sharp peak. While pure resonance is often linked to constructive interference, it is important to note that this does not necessarily imply the typical constructive interference that results in increased signal amplitude. Interestingly, in aluminum, the majority of resonances identified using the $\cos(\varphi)$ method exhibit destructive interference. However, two specific points, classified as Type A (pure resonance) in the Flax et al. model, still show destructive interference due to the material's scattering properties, despite their Type A classification. Similarly, for PLA at $ka = 3.73$, the resonance is classified as Type A (pure resonance) according to the Flax et al. model, which would typically suggest constructive interference. Nonetheless, the $\cos(\varphi)$ method predicts destructive interference at this point, highlighting a discrepancy due to the unique scattering characteristics of PLA. In summary, while both aluminum and PLA exhibit Type A (Pure Resonance), their interference behavior differs. Aluminum shows overall destructive interference, while PLA at $ka = 3.73$ demonstrates destructive interference, despite being classified as Type A in the Flax et al. model.

B. Experimental results

An aluminum rod and a PLA filament were prepared according to the specifications in Table 1. Figure 13 shows the backscattered signal from the samples at normal incidence, with a time offset applied; the actual time is obtained by adding a fixed offset value.

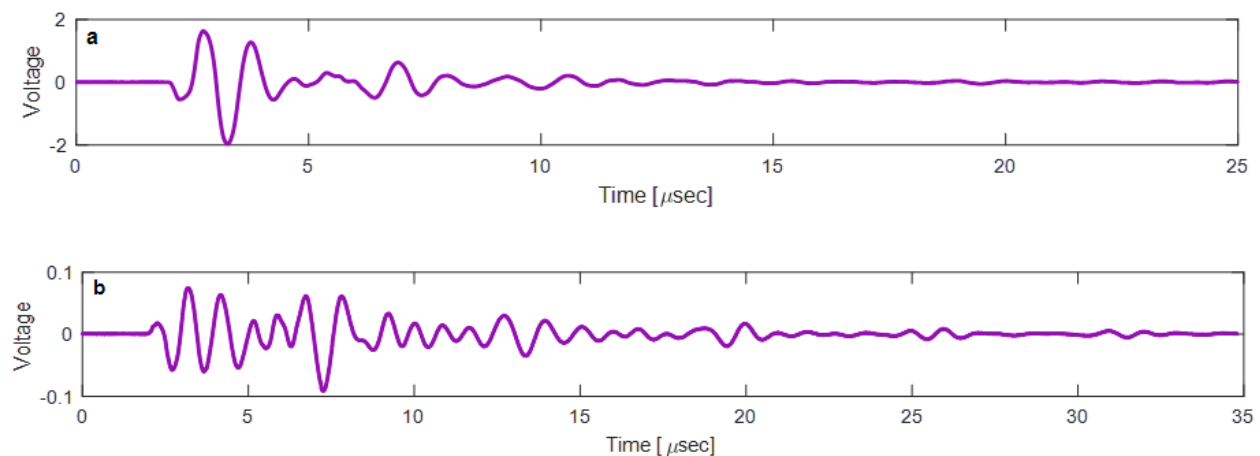


Fig. 13. Backscattered signals; a) aluminum, b) PLA

To extract the experimental form functions and eliminate the effects of the measurement system, the approach proposed by Sodagar et al. [26] is used. After deconvolution, the FFT is applied to this signal. The experimental form function for the aluminum sample is shown in Figure 14.

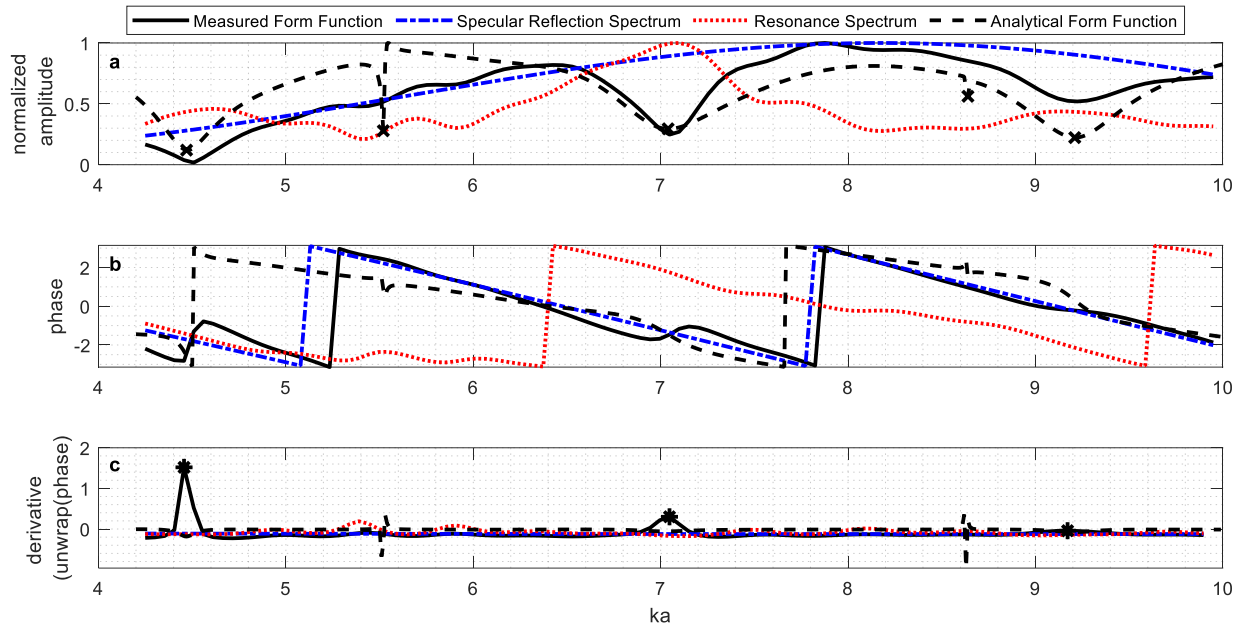


Fig. 14. Experimental graphs for the aluminum cylinder: a) amplitude plots of the form function, rigid background, and resonance spectrum; b) phase plots of the form function, rigid background, and resonance spectrum; c) derivative of the unwrapped phase plots of the form function, rigid background, and resonance spectrum.

Figure 14 and its subplots mirror the process used for plotting Figure 3. The data in Table 5 are directly derived from Figure 14 and align precisely with the information in Table 2.

The minima of the form function (potential resonances) are listed in Table 5. The range of ka values on the horizontal axis in Figure 14 is chosen based on the bandwidth of the 1-megahertz probe (500 kHz to 1.5 MHz) used in the experimental measurements.

This approach allows for a practical application of the theoretical insights into resonance phenomena, adapting the methodology to the specific constraints and capabilities of the experimental setup.

Similar to the observations in the analytical graphs (Section 4-A), the experimental study also shows that the minima of the form function correspond to the maxima of the resonance graph, and the interferences at these points are all destructive. Additionally, $ka = 5.52$ and $ka = 8.64$, which had very narrow resonance widths (approximately 0.05) in the analytical graphs, are not observed in the experimental outputs due to resolution constraints.

Table 5. Description of the extreme points of the experimental form function of the aluminum cylinder

ka	Position on form function	Position on rigid response	Position on the resonance spectrum	Interference type	Resonance width	(n, l)
4.51	Min.	Non.Peak	Max.	Destructive	1.14	(2,1)
5.39	Min.	Non.Peak	Max.	Destructive	5.7	-
5.86	Min.	Non.Peak	Max.	Destructive	5.7	-
7.05	Min.	Non.Peak	Max.	Destructive	1.60	(3,1)
8.19	Min.	Max.	Max.	Destructive	4.46	-
9.22	Min.	Non.Peak	Max.	Destructive	5.7	(4,1)

To facilitate the comparison between the analytical and experimental form functions, the analytical form function is plotted with a dashed line in Figure 14. This not only demonstrates a very good match between them but also highlights the cross-marked points representing the analytical resonance points.

The procedure conducted for the aluminum cylinder is also followed for the PLA filament to provide the experimental form function as displayed in Figure 15. Similarly, for the new material, the range of ka values in Figure 15 was selected based on the probe's bandwidth.

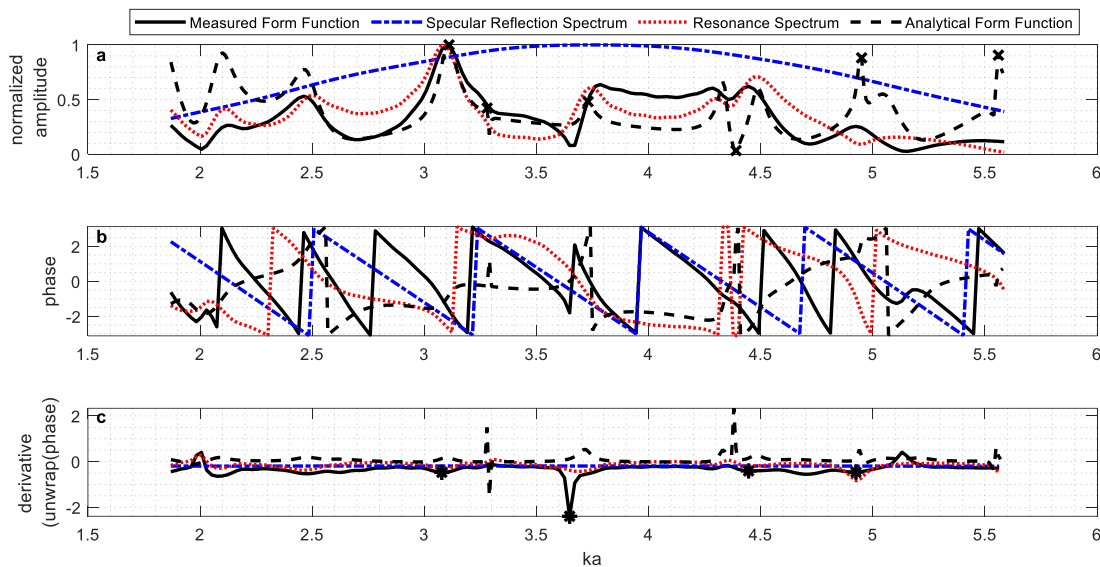


Fig. 15. Experimental graphs of the PLA filament; a) amplitude plots of the form function, rigid background, and resonance spectrum; b) phase plots of the form function, rigid background, and resonance spectrum; c) derivative of the unwrapped phase plots of the form function, rigid background, and resonance spectrum.

The ka values corresponding to the minima and maxima of the form function in Figure 15 are listed in Table 6.

Table 6. Description of the extreme points of the experimental form function of the PLA filament

ka	Position on form function	Position on rigid response	Position on the resonance spectrum	Interference type	Resonance width	(n, l) based on analytical function
2.46	Max.	Non.Peak	Max.	Constructive	1.319	(4,1)
3.10	Max.	Non.Peak	Max.	Constructive	1.28	(5,1)
4.92	Max.	Non.Peak	Min.	Destructive	3.648	(8,1)
3.65	Min.	Non.Peak	Max.	Destructive	1.14	(6,1)
4.35	Min.	Non.Peak	Min.	Constructive	1.231	(7,1)

As explained in Section 2, the experimental results also show that the maxima of the form function correspond to the polymer sample's resonance frequencies, with most points also being maxima in the resonance function, except for two cases. The resonances correspond to $ka = 3.29$ and $ka = 5.56$, which are very sharp in the analytical form function, and are not detected in the experimental form function. Additionally, some phase interferences in the experimental results are destructive, unlike the analytical results. These discrepancies between theoretical predictions and experimental measurements in this study stem from several factors inherent to the materials and experimental methods employed. Firstly, limitations in the resolution of the experimental setup can obscure the detection of sharp resonance points predicted theoretically, particularly in materials like PLA with high damping, where resonance peaks are less pronounced. Secondly, variability in the PLA material, influenced by manufacturing conditions and impurities, introduces deviations between predicted and measured resonance frequencies. This variability significantly affects acoustic wave propagation and interactions within PLA, complicating precise alignment with theoretical expectations during experimental testing. Lastly, the inherent damping characteristics of PLA broaden resonance peaks compared to metals such as aluminum, making them less distinct and challenging to detect precisely in experiments. These challenges underscore the complexities in translating theoretical insights into experimental outcomes, emphasizing the need for meticulous experimental design and analysis to enhance the reliability and accuracy of acoustic wave scattering studies in additive manufacturing and materials science applications.

Beyond these factors, additional sources of discrepancy may include acoustic boundary effects introduced by the experimental setup. Factors such as transducer positioning, alignment precision, and acoustic coupling with the surrounding medium can lead to deviations from idealized theoretical predictions. Small misalignments or imperfections in coupling may cause variations in observed resonance frequencies and amplitudes. Moreover, theoretical calculations assume an idealized infinite frequency resolution, whereas experimental measurements rely on discrete sampling and signal processing techniques such as windowing and filtering. These processing

steps may affect the detection and resolution of certain resonance peaks, particularly those with narrow bandwidths.

Another important aspect is wave-mode conversions and scattering artifacts. In real experimental conditions, interactions between different acoustic wave modes can lead to mode conversions that are not fully captured in analytical models. This effect is more pronounced in materials like PLA, where complex viscoelastic properties influence wave propagation. Additionally, unintended scattering from structural components of the experimental setup, such as holders or fixtures, may contribute to background noise and minor deviations in the measured form function.

Finite sample length effects can also influence the observed resonance behavior, as real samples are not truly infinite. While the theoretical model assumes an infinitely long cylinder, experimental samples are finite in length, which may introduce additional diffraction effects not accounted for in the theoretical predictions. Despite these factors, the experimental results still show a strong correlation with theoretical expectations, reinforcing the validity of the analysis.

The absence of certain sharp points in the experimental form function, which are present in the analytical function, suggests that real-world conditions or limitations of the experimental setup might affect the observation of these resonances. This discrepancy could also be linked to resonance widths: the broader resonance peaks in the experimental data might result from limitations in resolution or the system's damping, rather than the idealized sharp peaks in the analytical model.

The discrepancy in phase interference between the analytical and experimental results underscores the importance of considering practical factors in resonance analysis, such as the characteristics of the signal processing or measurement system used. Understanding these differences is crucial for accurately interpreting the material's behavior and can provide insights into refining experimental techniques or theoretical models to better align with actual material properties.

Unlike earlier work [29], which focused solely on modulus extraction via phase-derivative analysis, this study emphasizes resonance classification and interference behavior in both metallic and polymeric cylinders within a broader theoretical and experimental framework.

Table 7 compares the theoretical and experimental ka values, highlighting the discrepancies and the corresponding error margins observed in the measurements. It is important to note that the strict far-field criterion was not fully met in the experimental setup, and instead, a less restrictive quasi-far-field condition was applied. While this approximation is commonly used in similar acoustic studies, it can introduce spatial non-uniformities in the pressure field, which may affect the measured form function. Specifically, operating in the quasi-far-field or near-field regions can lead to slight shifts in peak locations and minor changes in amplitude, potentially contributing to the discrepancies between the experimental and theoretical results. These deviations from the ideal plane-wave model could explain some of the observed variations in the experimental data, especially in peak locations and the form function shape. Thus, the quasi-far-field condition should be considered as a possible source of error in the measurements.

Table. 7. Comparison between theoretical and experimental *ka* values of the aluminum cylinder and PLA filament

Aluminum cylinder			PLA filament		
Experimental <i>ka</i>	Theoretical <i>ka</i>	Error %	Experimental <i>ka</i>	Theoretical <i>ka</i>	Error %
-	-	-	2.46	2.46	0.00%
-	-	-	3.10	3.11	-0.32%
4.51	4.47	0.89%	3.65	3.73	-2.19%
5.39	5.52	-2.41%	-	4.34	-
5.86	-	-	4.92	4.95	-0.61%
7.05	7.04	0.14%	-	5.56	-
8.19	8.64	-5.49%	-	3.29	-
9.22	9.21	0.11%	4.35	4.39	-0.92%

Notably, the primary sources of uncertainty in this study include alignment errors, material property variations, and temperature fluctuations, all of which can impact resonance measurements. Instrumental precision also contributes to uncertainty in the calculated *ka* values. The percentage error between experimental results and model predictions is provided in Table 7, quantifying the extent of these uncertainties.

5. Conclusion

This investigation significantly advances the comprehension of the scattering characteristics and resonance frequencies observed in polymeric filament samples. Noteworthy is the revelation that, under the specific conditions of this study, resonance frequencies within a metallic cylinder (aluminum) predominantly correspond to the minima of the form function. In contrast, within a PLA, they mostly align with the maxima. Such insights deepen the understanding of resonance phenomena during the scattering of acoustic waves across different materials, revealing a contrasting nature of interference: destructive in aluminum, where resonance frequencies typically coincide with the form function minima, and constructive in PLA, where resonance frequencies align with the form function maxima. This observation underscores that the nature of resonance at these points is due to interference patterns.

Furthermore, it is important to note that the observation of very sharp resonances, due to damping and experimental limitations, has been elusive. These points of resonance typically exhibit very narrow bandwidths.

These findings lay a foundation for further investigations, inviting refinement of theoretical models and experimental techniques to capture the intricacies of material behaviors. Such advancements

hold promise for various applications, including material characterizations, across a spectrum of fields, particularly in additive manufacturing.

To strengthen the depth and breadth of the current study, several additional analyses are proposed. Broadening the scope to include larger-diameter cylinders would enable exploration across a wider range of ka values, thereby bolstering the reliability of the current findings. Furthermore, investigating the scattered fields from obliquely incident waves would enable identification of the anisotropic properties of cylindrical polymeric filaments.

Regarding model limitations, the acoustic scattering model used in this study is purely elastic, which does not apply to PLA due to its viscoelastic nature and significant internal acoustic damping. The primary objective of this paper, however, is to extract the baseline elastic properties (longitudinal and shear wave velocities) from measured resonance frequencies (ka), which is successfully achieved using the elastic model. However, high viscoelastic damping in PLA is a major limitation, as it affects the amplitude and width of the peaks and, to a very small degree, their exact center frequencies. This damping is considered one of the reasons for the discrepancies observed in the PLA cylinder results. It causes significant peak broadening, reducing the quality factor Q and rendering several sharp, high- Q analytical resonances undetectable within the experimental noise floor, especially at higher ka values. Although a complete viscoelastic analysis is desirable, it requires frequency-dependent material data beyond the scope of the current study.

Author declarations

Conflict of interest

The authors declare that they have no known competing financial interests or personal relationships that could have appeared to influence the work reported in this paper.

Data availability

Data will be made available on request.

Credit authorship contribution statement

Vajihehsadat Sajadi: Methodology, Validation, Data curation, Software, Writing – original draft preparation. Farhang Honarvar: Conceptualization, Validation, Writing – review & editing, Supervision. Mohammadreza Kari: Experimental design, Resources, Validation, Assistance in data acquisition and analysis, Writing – review & editing.

Declaration of generative AI and AI-assisted technologies in the writing process

During the preparation of this work the authors used ChatGPT in order to check for spelling, grammar, sentence structure and terminology and ensure that their work is written in correct English before submission. After using this tool/service, the authors reviewed and edited the content as needed and take full responsibility for the content of the publication.

References

- [1] L. Flax, L. Dragonette, H. Überall, Theory of elastic resonance excitation by sound scattering, *The Journal of the Acoustical Society of America*, 63 (1978) 723-731.
- [2] G. Maze, B. Taconet, J. Ripoché, Influence des ondes de “galerie a echo” sur la diffusion d'une onde ultrasonore plane par un cylindre, *Physics letters A*, 84 (1981) 309-312.
- [3] J.J. Faran, Sound scattering by solid cylinders and spheres, *The Journal of the acoustical society of America*, 23 (1951) 405-418.
- [4] L. Flax, V. Varadan, V. Varadan, Scattering of an obliquely incident acoustic wave by an infinite cylinder, *The Journal of the Acoustical Society of America*, 68 (1980) 1832-1835.
- [5] F. Honarvar, A. Sinclair, Acoustic wave scattering from transversely isotropic cylinders, *The Journal of the Acoustical Society of America*, 100 (1996) 57-63.
- [6] F. Ahmad, A. Rahman, Acoustic scattering by transversely isotropic cylinders, *International Journal of Engineering Science*, 38 (2000) 325-335.
- [7] H. Rhee, Y. Park, Novel acoustic wave resonance scattering formalism, *The Journal of the Acoustical Society of America*, 102 (1997) 3401-3412.
- [8] B.T. Hefner, P.L. Marston, Backscattering enhancements associated with subsonic Rayleigh waves on polymer spheres in water: Observation and modeling for acrylic spheres, *The Journal of the Acoustical Society of America*, 107 (2000) 1930-1936.
- [9] L.S. Schuetz, W.G. Neubauer, Acoustic reflection from cylinders—nonabsorbing and absorbing, *The Journal of the Acoustical Society of America*, 62 (1977) 513-517.
- [10] F.G. Mitri, E. Zine El Abidine, J.-Y. Chapelon, Acoustic backscattering form-function of absorbing cylinder targets, *Journal of the Acoustical Society of America*, 115 (2004) 1411-1413.
- [11] K.L. Williams, P.L. Marston, Synthesis of backscattering from an elastic sphere using the Sommerfeld–Watson transformation and giving a Fabry–Perot analysis of resonances, *The journal of the acoustical society of America*, 79 (1986) 1702-1708.
- [12] N. Sun, P. Marston, Ray synthesis of leaky Lamb wave contributions to backscattering from thick cylindrical shells, *The Journal of the Acoustical Society of America*, 91 (1992) 1398-1402.
- [13] F. Mitri, J. Greenleaf, Z.E.A. Fellah, M. Fatemi, Investigating the absolute phase information in acoustic wave resonance scattering, *Ultrasonics*, 48 (2008) 209-219.
- [14] P.L. Marston, GTD for backscattering from elastic spheres and cylinders in water and the coupling of surface elastic waves with the acoustic field, *The Journal of the Acoustical Society of America*, 83 (1988) 25-37.
- [15] P.L. Marston, Leaky waves on weakly curved scatterers. II. Convolution formulation for two-dimensional high-frequency scattering, *The Journal of the Acoustical Society of America*, 97 (1995) 34-41.
- [16] H. Batard, G. Quentin, Acoustical resonances of solid elastic cylinders: Parametric study and introduction to the inverse problem, *The Journal of the Acoustical Society of America*, 91 (1992) 581-590.
- [17] F. Honarvar, A. Sinclair, Nondestructive evaluation of cylindrical components by resonance acoustic spectroscopy, *Ultrasonics*, 36 (1998) 845-854.

- [18] M. Kari, F. Honarvar, Nondestructive characterization of materials by inversion of acoustic scattering data, *Inverse Problems in Science and Engineering*, 22 (2014) 814-831.
- [19] M. Kari, F. Honarvar, Characterization of a cylindrical rod by inversion of acoustic scattering data, *Ultrasonics*, 54 (2014) 1559-1567.
- [20] F. Honarvar, E. Enjilela, Resonance acoustic spectroscopy, in: *Handbook of Applied Solid State Spectroscopy*, Springer, 2006, pp. 351-409.
- [21] N.D. Veksler, *Resonance acoustic spectroscopy*, Springer Science & Business Media, 2012.
- [22] S.G. Kargl, P.L. Marston, Background contributions and coupling coefficients for backscattering by thick shells, *The Journal of the Acoustical Society of America*, 101 (1997) 3792-3797.
- [23] S. Numrich, W. Howell, J. Subrahmanyam, H. Überall, Acoustic ringing response of the individual resonances of an elastic cylinder, *The Journal of the Acoustical Society of America*, 80 (1986) 1161-1169.
- [24] D. Halliday, R. Resnick, J. Walker, *Fundamentals of physics*, John Wiley & Sons, 2013.
- [25] F.D.C. Siacor, Q. Chen, J.Y. Zhao, L. Han, A.D. Valino, E.B. Taboada, E.B. Caldon, R.C. Advincula, On the additive manufacturing (3D printing) of viscoelastic materials and flow behavior: From composites to food manufacturing, *Additive Manufacturing*, 45 (2021) 102043.
- [26] S. Sodagar, F. Honarvar, A. Yaghootian, A.N. Sinclair, An alternative approach for measuring the scattered acoustic pressure field of immersed single and multiple cylinders, *Acoustical Physics*, 57 (2011) 411-419.
- [27] H. Überall, Surface waves in acoustics, in: *Physical acoustics*, Elsevier, 1973, pp. 1-60.
- [28] T. Suzuki, An overview of full width at half maximum, in: <https://www.pulstec.net/what-is-full-width-at-half-maximum> (Ed.), 2024.
- [29] V. Sajadi, F. Honarvar, M. Kari, Utilizing the derivative of unwrapped phase in ultrasonic nondestructive evaluation of elastic properties of polymer filaments, *The Journal of the Acoustical Society of America*, 155 (2024) 1391-1405.
- [30] D.S. Plotnick, P.L. Marston, T.M. Marston, Fast nearfield to farfield conversion algorithm for circular synthetic aperture sonar, *The Journal of the Acoustical Society of America*, 136 (2014) EL61-EL66.
- [31] B.R. Hall, P.L. Marston, Backscattering by a tilted intermediate thickness cylindrical metal empty shell in water, *JASA Express Letters*, 2 (2022).